ACS APPLIED MATERIALS & INTERFACES

Research Article

www.acsami.org

Photocatalytic Degradation of Methyl Orange over Nitrogen–Fluorine Codoped TiO_2 Nanobelts Prepared by Solvothermal Synthesis

Zuoli He, Wenxiu Que,* Jing Chen, Xingtian Yin, Yucheng He, and Jiangbo Ren

Electronic Materials Research Laboratory, School of Electronic and Information Engineering, and International Center for Dielectric Research, Xi'an Jiaotong University, Xi'an 710049, Shaanxi, People's Republic of China

Supporting Information

ABSTRACT: Anatase type nitrogen–fluorine (N–F) codoped TiO_2 nanobelts were prepared by a solvothermal method in which amorphous titania microspheres were used as the precursors. The as-prepared TiO_2 nanobelts are composed of thin narrow nanobelts and it is noted that there are large amount of wormhole-like mesopores on these narrow nanobelts. Photocatalytic activity of the N–F codoped TiO_2 nanobelts was measured by the reaction of photocatalytic degradation of methyl orange. Results indicate that the photocatalytic activity of the N–F codoped TiO_2 nanobelts is higher than that of P25, which is mainly ascribed to wormhole-like mesopores like prison, larger surface area, and enhanced absorption of light due to N–F codoping. Interestingly, it is also found that the photocatalytic activity can be further enhanced when tested in a new testing method because more photons can be captured by the nanobelts to stimulate the formation of the hole–electron pair.

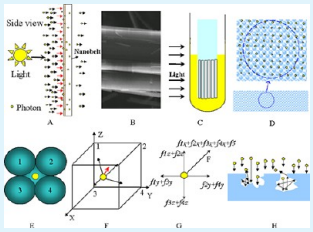

KEYWORDS: *TiO_2 nanobelt, mesopores, photocatalytic activity, N–F codoped, solvothermal method*

1. INTRODUCTION

Semiconductor photocatalysis has been extensively studied in recent years from the viewpoint of environmental accountability and energy conversion.[1−3] Because of its unique physicochemical properties, one-dimensional TiO_2-related materials have aroused much interest lately in the areas of photocatalysis.[4,5] As one knows, one-dimensional (1D) TiO_2-related materials with high morphological specificity, such as nanotubes, nanowires, nanobelts, and nanofibers have attracted particular attention because of their unique microstructure and promising functions.[6,7] Especially, one-dimensional nanostructures have many great advantages over nanospheres or nanoparticles as follows: (1) scattering and absorption of visible light are highly enhanced in 1D nanostructure because of their high length-to-diameter ratio;[6,8,9] (2) 1D geometry facilitates rapid diffusion-free electron transport along the longest direction;[6,9−11] (3) high degree of crystallinity of the nanowires/nanobelts and low number of grain boundaries may exhibit a lower recombination rate;[6,9] (4) smaller pore size and larger surface area, which may increase absorption of photons and the photons may collide with the nanobelts and thus energy exchange exists in this collision. Moreover, one-dimensional nanostructures have some potential to exhibit unusual properties and offer opportunities to investigate physical and chemical processes in size-confined systems.[12,13] Investigations on the effect of the aspect ratio and pore size on the photocatalytic performances of photocatalysts are indispensable. As we consider this, the nanobelts should show better performance in photocatalystic activity among the one-dimensional (1D) nanomaterials.

For environmental purposes, especially in application to the degradation of the environmental pollutants, the photocatalytic reactions take place on the surface and thus the surface properties of the photocatalysts play a critical part in determining reaction efficiencies and mechanisms.[5] Surface properties of TiO_2 are related with many parameters such as morphology, nanostructure, surface hydroxyl group, particle size, crystalline phase, surface defect, and pores size. As we have reported, TiO_2 surfaces have been actively modified through manipulating the above parameters in order to optimize or control the photocatalytic reactions. In recent research, modified TiO_2, such as N-doped TiO_2, has been examined in order to extend the absorption edge into the visible light region and show some enhancement in photocatalytic activity,[6,13−17] and Wang pointed that nitrogen doping allows visible-light-responsive photocatalytic activity, but lowers UV-light-responsive photocatalytic activity.[6] The visible-light photocatalytic activity originates from the N 2p levels near the valence band, and the oxygen vacancies and the associated Ti^{3+} species act as the recombination centers for the photoinduced electrons and holes. They reduce the photocatalytic activity although they contribute to the visible light absorbance.[6,16] Fluorinated TiO_2 has been also investigated in relation to doping ($TiO_{2-x}F_x$) or surface complexation (F-TiO_2),[18,19] which reported that F-doping in TiO_2 can also enhance photocatalytic activity by the creation of oxygen vacancies,[20,21]

Received: September 14, 2012
Accepted: November 13, 2012
Published: November 13, 2012

   dx.doi.org/10.1021/am3019965 | ACS Appl. Mater. Interfaces 2012, 4, 6816–6826

actually, F-doping can improve crystallinity of anatase and photocatalytic reactivity.[18] The F-doped TiO_2 also shows stronger absorption in the UV−visible range and a red shift in the band gap transition.[22] Recently, many research papers have reported the N−F codoped TiO_2 powders and their enhanced photocatalytic activity.[23−31] The N−F codoped TiO_2 shows a higher absorption and higher water splitting activity than the N-doped TiO_2 under visible light.[23,27,28,30,31] Huang[29] pointed that the high activity is ascribed to a synergetic effect of the doped nitrogen and fluorine atoms, that is to say, the doped N atoms improve the visible-light absorption and the doped F atoms lead to the enhancement of the surface acidity, which can increase the adsorption of the reactant and thus further enhances the photocatalytic activity. It should be mentioned that F-doping might also lead to the formation of a new active site.[29]

Herein, we reported the preparation of the N−F codoped TiO_2 nanobelts and their photocatalytic activities. To optimize the photocatalytic activity of the N−F codoped TiO_2 nanobelts, we investigated the chemical status and electronic structure, Barrett−Joyner−Halenda (BJH) pore size distribution and surface area, light absorption of the TiO_2 nanobelts. Results demonstrate that a significantly enhanced photocatalytic activity is related to above these factors and a surprising enhancement of the photocatalytic activity is believed to be facilitated by the inherent surface photocatalytic behavior of TiO_2 when exposed to UV or visible light. In addition, we investigated the effect of the aspect ratio and pore size on the photocatalytic performances of the nanobelts photocatalysts. We presented a new method to optimize this behavior and result indicates that the photocatalytic activity of the codoped samples can be further enhanced, and we also proposed a model named "Prison Break" to explain this.

2. EXPERIMENTAL SECTION

2.1. Preparation. In our experiment, tetrabutyl titanate ($Ti(OBu)_4$), ethanol, sodium chloride, sodium hydroxide, ammonium fluoride, and P25 (Degussa, German, CAS no. 13463−67−7, surface area (BET) 50 ± 15 m^2/g, average grain diameter 21 nm) were of analytical grade without further purification. Deionized water was used throughout the preparation.

Typical experimental procedures are as follows as shown in Figure 1A: First, 2.2 mL of $Ti(OBu)_4$ was added dropwise into a mixture of ethanol (100 mL) and sodium chloride solution (0.4 mL 0.1M) to obtain a turbid solution under a magnetic stirring. Then, the suspension was aged in a static condition for 24 h. Followed that the powder deposited at the bottom of the vessel was collected and dried at 80 °C in air. This product was defined as sample 1 (S1) and used as precursor for next step. Second, 0.8 g of the as-prepared nanoparticles (S1) and 0.37 g ammonium fluoride were dispersed into 50 mL of 10 M sodium hydroxide solution with an assistance of strong magnetic stirring. After being stirring about 30 min, the final mixture was directly transferred into a 100 mL Teflon stainless autoclave. The autoclave was maintained in oven at 180 °C for 72 h and then cooled down to room temperature. White solid powders were thus obtained by washing with ethanol and deionized water several times and dried in the air at 80 °C. Also, the N−F-codoped TiO_2 nanobelts were finally prepared.

2.2. Characterization. Crystalline properties of the as-prepared samples were characterized by powder X-ray diffractometry (D/max-2200, Rigaku, Japan) using Cu Kα radiation. Morphologies of the products were observed by using a high resolution field emission environmental scanning electron microscope (JSM-7000) coupled with an energy-dispersive X-ray (EDX) spectrometer, all the images were obtained under high vacuum mode without sputter coating. Composition of the products was performed using X-ray photoelectron spectroscopy (XPS), which were obtained by Axis Ultra, Kratos (UK) using monochromatic Al Kα radiation (150 W, 15 KV, 1486.6 eV) under a vacuum pressure of 10^{-9} Torr. All the binding energies were referenced to the C1s peak (284.80 eV) from hydrocarbons adsorbed on the surface of the samples. Special surface area of the products was calculated by using Brunauer−Emmett−Teller (BET) model from a linear part of BET plot (P/P_0 = 0.10−0.30), and average pore diameter was calculated by the Barrett−Joyner−Halenda (BJH) method from the desorption branch of isotherm. UV−vis absorption spectra of the TiO_2 powders were obtained from the dry-pressed disk samples by using a UV−vis spectrophotometer (Lambda 950, PerkinElmer).

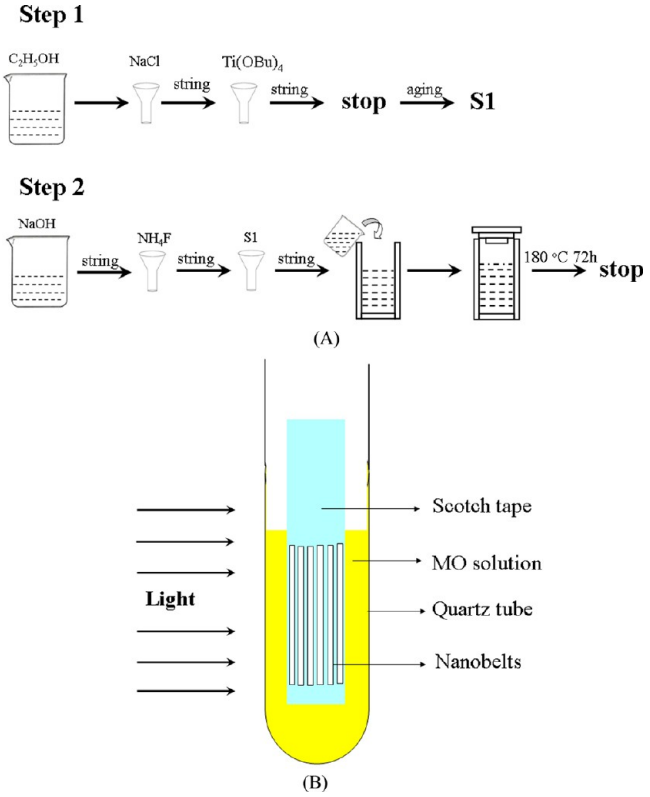

Figure 1. (A) Synthetic route for preparing the N−F codoped TiO_2 nanobelts. (B) Schematic illustration of the new testing method for photocatalytic activity of the TiO_2 nanobelts.

2.3. Photocatalytic Activity Measurement. Methyl orange (MO), which is a kind of the dye known to be carcinogenic and mutagenic, was usually selected as a model dye to evaluate the photocatalytic performance of different photocatalysts. Here, the photocatalytic activity of the as-prepared photocatalysts was evaluated by the decomposition of the MO in a deionized water solution with an initial concentration of 20 mg/L. To evaluate the photocatalytic activity of the photocatalysts, we carried out a series of normal tests as follows: 0.02 g of TiO_2 photocatalysts were added into 100 mL of 20 mg/L MO solution, dispersed by a sonicating for 10 min, and stirred by a magnetic bar for another 10 min to reach the adsorption−desorption equilibrium. Then the suspension solution was transferred to quartz tubes and illuminated by an UV light with a 300 W high-pressure mercury lamp. Magnetic stirring was carried out during the photocatalytic testing. The whole system including the mercury lamp and reactant suspension solution was maintained at room temperature by a flow of cooling water. Certain volume of the dye suspension solutions was withdrawn at a sequence of time intervals. Photodegradation of the MO as a model endocrine disrupting compound was also investigated under visible solar irradiation ($\lambda \geq 420$ nm). A solar simulator with a 500 W xenon arc lamp equipped with an air mass filter (AM 1.5G) with a special UV cutoff filter ($290 < \lambda < 420$ nm) provided the visible-light source.

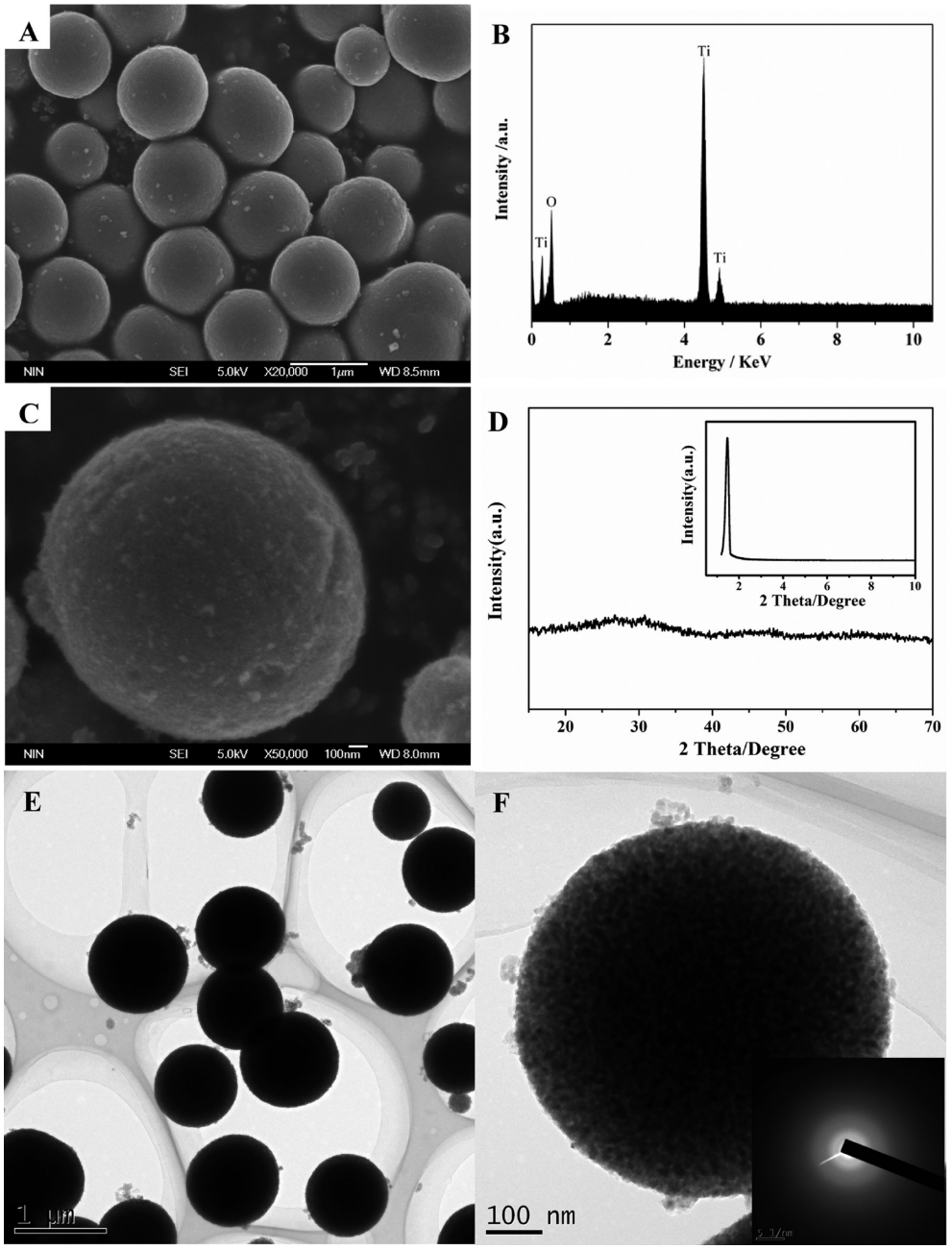

Figure 2. Physicochemical features of the TiO_2 precursor microspheres. (A, C) SEM images; (B) EDX spectrum; (D) XRD pattern; (E, F) TEM images and typical SAED patterns (F inset).

New testing method: The MO solution was also selected as the model dye with a concentration of 20 mg/L. 0.02g photocatalysts were dispersed into 20 mL of ethanol in the evaporating dish by the help of sonication, and then dried in the air at 80 °C. The powder deposited at the bottom of the evaporating dish was carried out and fixed by scotch tape. Then tried my best to put the tape with same photocatalysts into every quartz tubes with the same amount of the MO solution, and the covered photocatalysts tape side faced the incident light direction as shown in Figure 1B. Irradiation was under an UV light and visible solar irradiation, but it should be mentioned here that magnetic stirring was not carried out during this new testing process. After desired time intervals of irradiation, the supernatant liquid was collected and analyzed by recording the characteristic absorption of the MO (464 nm) using an UV−vis spectrophotometer (Lambda 950, PerkinElmer), and the value of the decomposition efficiency was calculated on the basis of the standard absorption curve of the concentration and absorption. The oxygen equivalent of the organic matter of a sample, i.e., chemical oxygen demand (COD), was measured by using a WTW photo S6 photometer. The reagents for COD analysis and 3 mL of a sample taken at different times were mixed together in glass cells and digested in a WTW CR 3200 Thermodigester for 2 h at 423 K. After digestion, the mixture was cooled to room temperature and the COD was measured by using the photometer. The COD was measured for the original solution and the centrifuged sample taken out at different time intervals.

3. RESULTS AND DISCUSSION

3.1. Physicochemical Features of Precursor. Physicochemical features of the precursor composed of monodispersed microspheres with a diameter of about 800 nm are shown in Figure 2. It can be observed that these microspheres are composed of many nanoparticles as shown in images A and C in Figure 2 and possess relatively smooth surfaces. Figure 2B is

dx.doi.org/10.1021/am3019965 | ACS Appl. Mater. Interfaces 2012, 4, 6816−6826

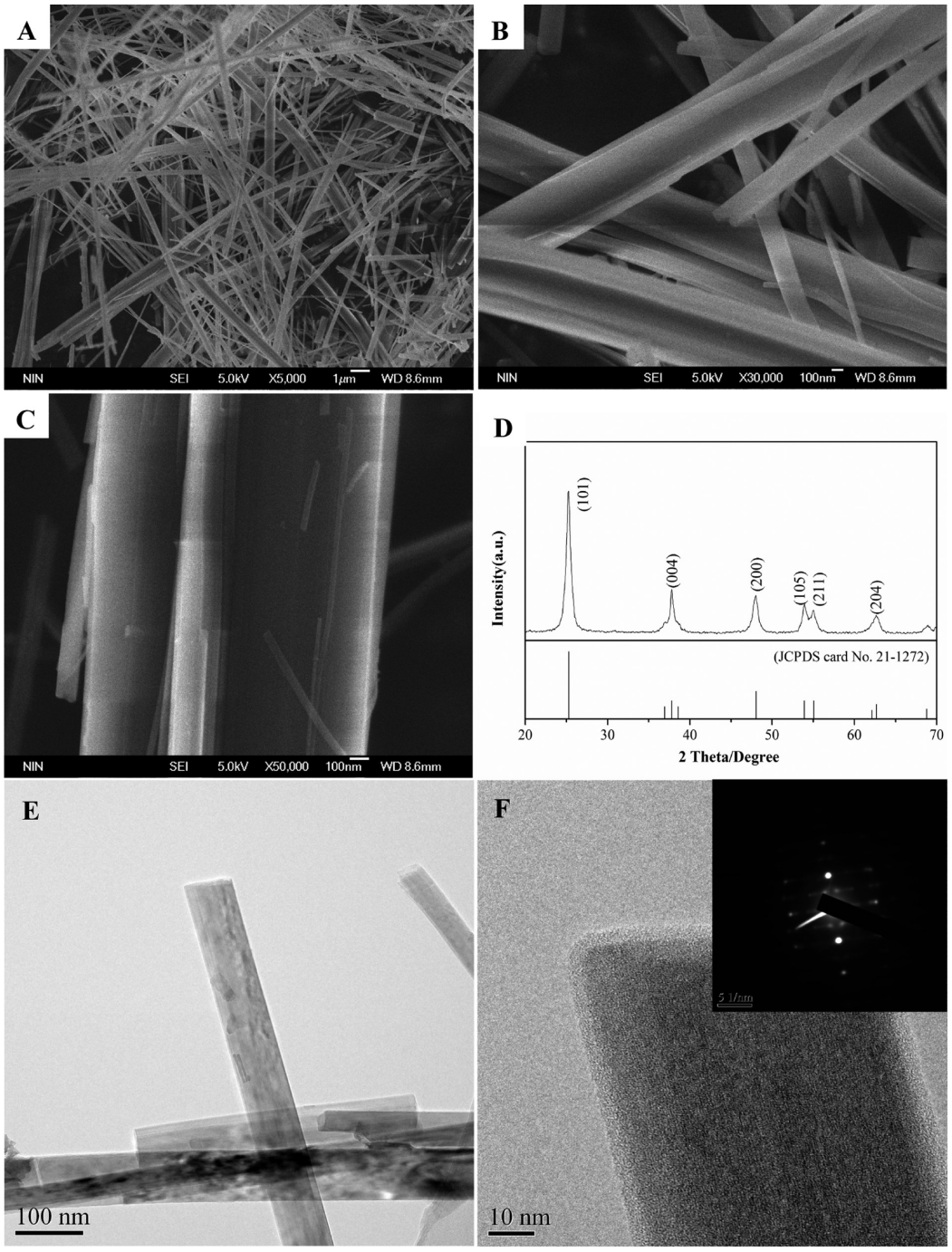

Figure 3. Physicochemical features of the N−F codoped TiO_2 nanobelts: (A−C) SEM images; (D) XRD pattern; (E, F) TEM images and typical SAED patterns (F inset).

an EDX spectrum of the TiO_2 microspheres, which only shows elements of O and Ti, that is to say, only Ti and O elements exist in the microspheres. The detailed elemental analysis is presented in Table S1 (see Table S1 in the Supporting Information), indicating that the excess of O may exist in O_2 or CO_2 and other gaseous oxides. The phase constitution and crystallite size of the samples were determined by X-ray diffractometry analysis using nickel filtered copper radiation (Cu Kα) at 30 kV, 30 mA over a 2θ range of 15−70°. Figure 2D shows XRD pattern of the precursor microspheres, indicating that these precursor microspheres are amorphous.

Morphologies of the as-prepared samples were further investigated by TEM observation and shown in images E and F in Figure 2, it can be clearly seen that the average diameter size of the microspheres is about 800 nm and the microsphere is composed of the nanoparticles, which confirms the results obtained by SEM. SAED pattern as an inset of Figure 2F shows that the TiO_2 precursor is an amorphous TiO_2 and without any crystal phases can be observed, which corresponds to the XRD results and further confirms that the precursor microspheres are amorphous.

3.2. Characterization of Morphology and Crystal Structure of the Nanobelts. Figure 3 shows the

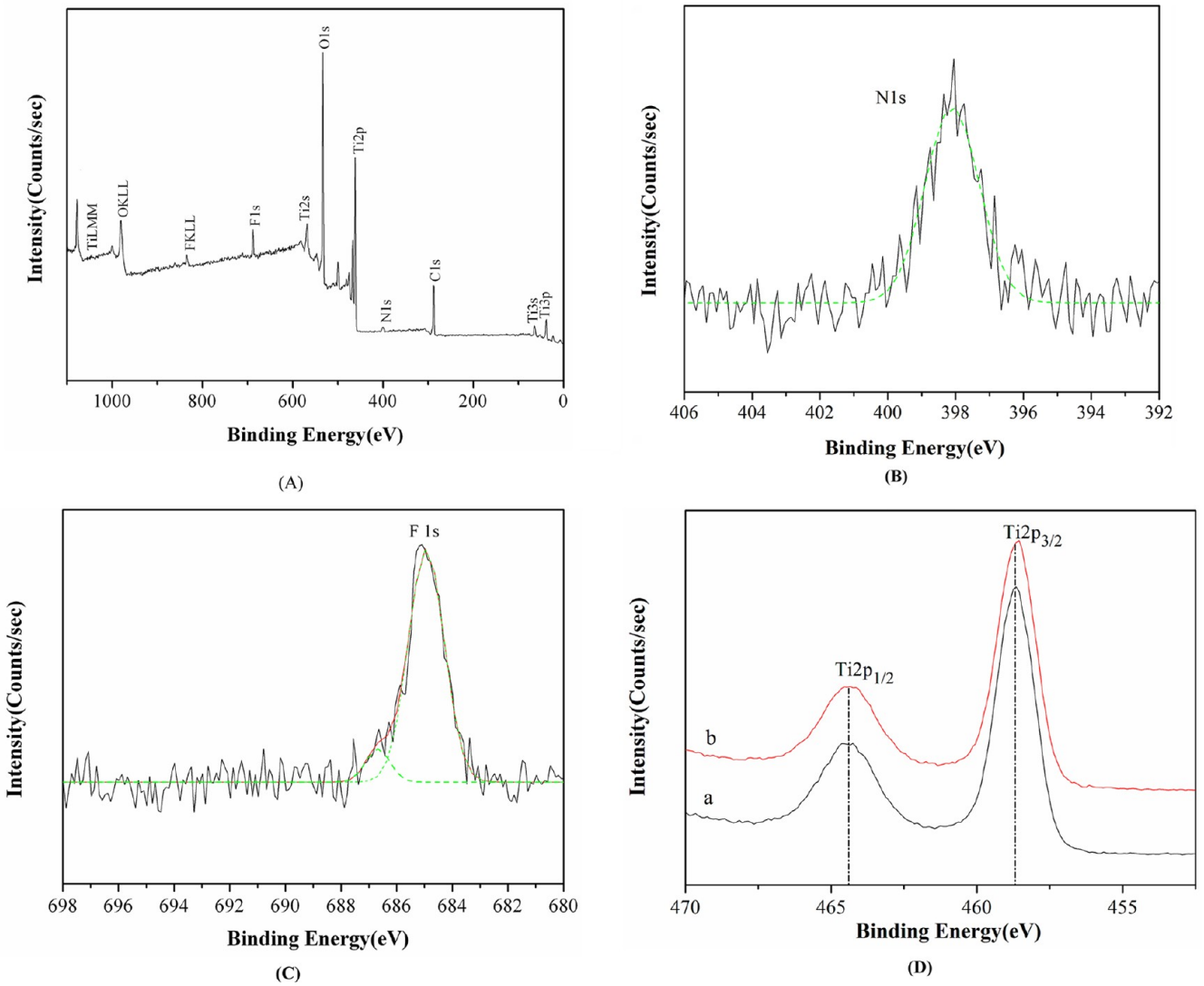

Figure 4. (A) Survey spectrum; (B) N1s XPS spectrum; (C) F1s XPS spectrum of the N−F codoped TiO_2 nanobelts, (D) Ti2p XPS spectra of the TiO_2 precursor microspheres (a) and the N−F codoped TiO_2 nanobelts (b).

Table 1. XPS Peak Position and the N and F Contents of the TiO_2 Products

samples	Ti 2p peak position BE(eV)	N 1s peak position BE(eV)	N content atomic conc. (%)	F 1s peak position BE(eV)	F content atomic conc. (%)
microspheres (S1)	2p1/2 464.39				
	2p3/2 458.68				
N−F codoped nanobelts	2p1/2 464.40	400.56	3.07	686.82	1.48
	2p3/2 458.53			684.88	

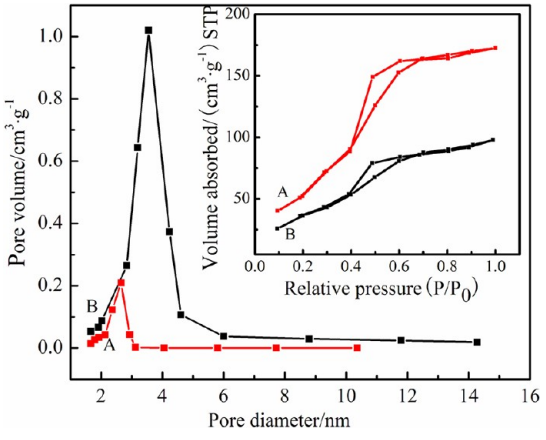

Figure 5. Barrett−Joyner−Halenda (BJH) pore size distribution and nitrogen adsorption/desorption isotherm (inset) of the TiO_2 products: (A) the N−F codoped nanobelts; (B) the precursor microspheres.

physicochemical features of the TiO_2 nanobelts obtained by the solvothermal processing. As seen from the SEM images, it can be observed that the nanobelts are 200−600 nm in width and up to tens of micrometers in length. Combining with the TEM observation, it can be concluded that the nanobelts are composed of the narrow nanobelts with about 100 nm in width and very thin in thick as shown in images C and E in Figure 3, and those narrow nanobelts attached on the surface of the nanobelts as observed in Figure 3C may be broken ones due to the ultrasonic dispersion treatment.

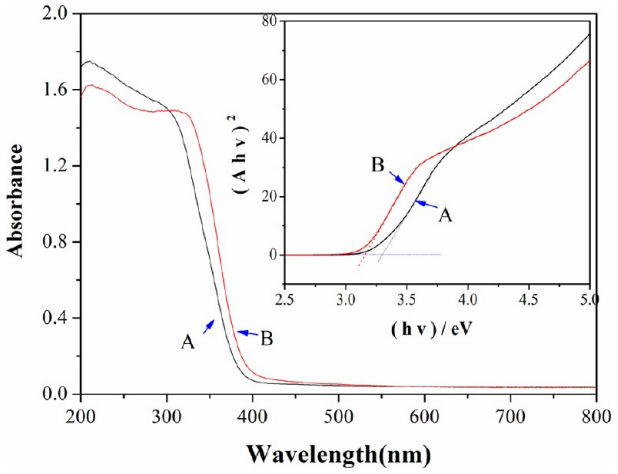

Figure 6. UV−visible absorption spectra of the TiO_2 products and the inset shows direct band gap estimation: (A) the undoped nanobelts; (B) the N−F codoped nanobelts.

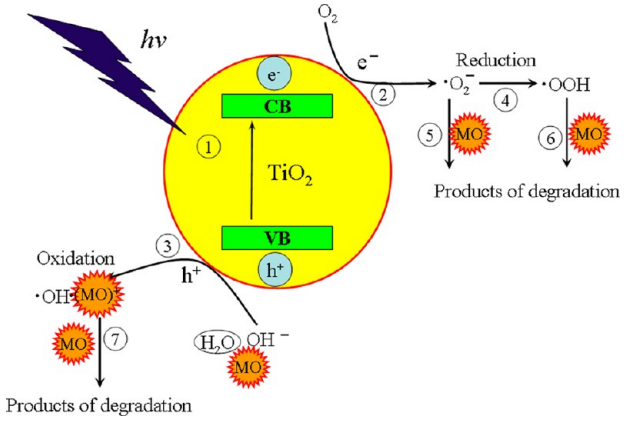

Figure 7. Schematic diagram of a possible mechanism of the degradation of the MO on the semiconductor photocatalyst surface under light irradiation.

Table 2. Degradation Rate Constant (k) Values for Different Photocatalysts

photocatalyst	K ($\times 10^{-4}$ min^{-1})	
	UV light irradiation	visible light irradiation
none	5	4
microspheres (S1)	14	9
P25	67	40
undoped nanobelts	82	47
co-doped nanobelts	93	60
co-doped nanobelts in new testing method	165	82

XRD analysis reveals that the TiO_2 nanobelts have a monolithic anatase structure (JCPDS card no. 21−1272) as shown in Figure 3D, the TiO_2 nanobelts are anatase single crystals with the growth direction along [010], which can be further confirmed by TEM analysis as shown in the inset of Figure 3F. It can be clearly seen from Figure 3E that the TiO_2 nanobelts are very thin, which is probably related to that the sample for TEM observation is dispersed by sonication, thus, it is possible that the nanobelts are broken into small piece and became more narrow, which is about 100 nm as seen in Figure 3E. As shown in the inset image of Figure 3F, the selective area diffraction data can be indexed to explain that the anatase single crystals have the preferential growth direction along (101) plane. The surface of the belts is shaggy, which shows an existence of the wormhole-like mesopores structure.

3.3. Measurement of Chemical Status and Electronic Structure by XPS. XPS measurement was performed on the N−F codoped TiO_2 nanobelts. Figure 4A shows the XPS spectrum of the N−F codoped TiO_2 nanobelts. It can be seen that the measured sample consists of Ti, O, C, N, and F, and the C is mainly ascribed to an adventitious hydrocarbon from XPS itself. Figure 4B shows the XPS spectrum of the N 1s region, whereas Figure 4C represents the F 1s region. The XPS spectrum of N 1s indicates that one peak of binding energy is around 400.56 eV, which most of the researchers interpret that the peaks above 400 eV are from the chemisorbed-N_2 or from surface adsorbed NHx species or from Ti−O−N or Ti−N−O oxynitride,[17,6] although there is still some controversy over the exact position of the N in TiO_2.[14] Figure 4C shows a high-resolution XPS spectrum of F1s. It can be seen that the F1s region is composed of two contributions. One symmetrical peak located at 684.88 eV should be originated from the fluorinated compounds adsorbed on the surface, and the small peak located around 686.82 eV is attributed to the F atoms doped in TiO_2, i.e., the substituted F atoms occupied oxygen sites in the TiO_2 crystal lattice.[27] It is reasonable to assume that the small peak is resulted from Ti−F bonds, indicating that the F atoms are incorporated into the TiO_2 crystal lattice via the solvothermal process.[33] The peak position of Ti $2p_{3/2}$ corresponds to that of the Ti^{4+} oxidation state as shown in Figure 4D, indicating that the shape of the Ti 2p excludes the presence of traceable amount of Ti^{4+}. The XPS spectrum of the Ti 2P core level obtained from the TiO_2 precursor microspheres exhibits a Ti $2P_{3/2}$ peak at 458.68 eV. After a treatment in autoclave at 180 °C for 72 h, the Ti $2P_{3/2}$ peak shifts to 458.53 V as presented in Table 1. The shift of the Ti $2P_{3/2}$ is mainly due to the introduction of oxygen vacancies into the TiO_2 lattice.[6] In addition, the atomic content of nitrogen and fluorine in the N−F codoped product was also calculated from the XPS spectra, which N and F contents are 3.07 and 1.48 at %, respectively.

3.4. Measurement of BJH Pore Size Distribution and Surface Area. The obtained TiO_2 nanobelts show no significant order in pore arrangement. After the solvothermal treatment at low temperature of 180 °C for 72 h, the formation and afterward crystallite growth of the TiO_2 phase, together with the nanoparticle clustering and restricting increasing of the grain size, resulting in an increase of the wormhole-like mesopores dramatically. From the TEM images as seen in Figure 3F, the surface of the belts is shaggy, which shows an existence of the wormhole-like mesopores structure. The N_2 adsorption−desorption experimental results show that the pore volume and surface area of the nanobelts are at about 0.31 cc/g and 108.2 m^2/g, respectively, whereas the surface area of the precursor microspheres is about 65 m^2/g. Figure 5 shows the N_2 sorption isotherms and BJH pore size distribution curves of the samples, respectively. It can be seen that all isotherms are of typical type IV with hysteresis loop, indicating that the precursor microspheres and the N−F codoped nanobelts are both mesoporous materials. In addition, all samples display steep capillary condensation and evaporation steps within the pressure range of P/P_0 = 0.4−0.7, implying they have a narrow mesopore size distribution. These results can be also confirmed

dx.doi.org/10.1021/am3019965 | ACS Appl. Mater. Interfaces 2012, 4, 6816−6826

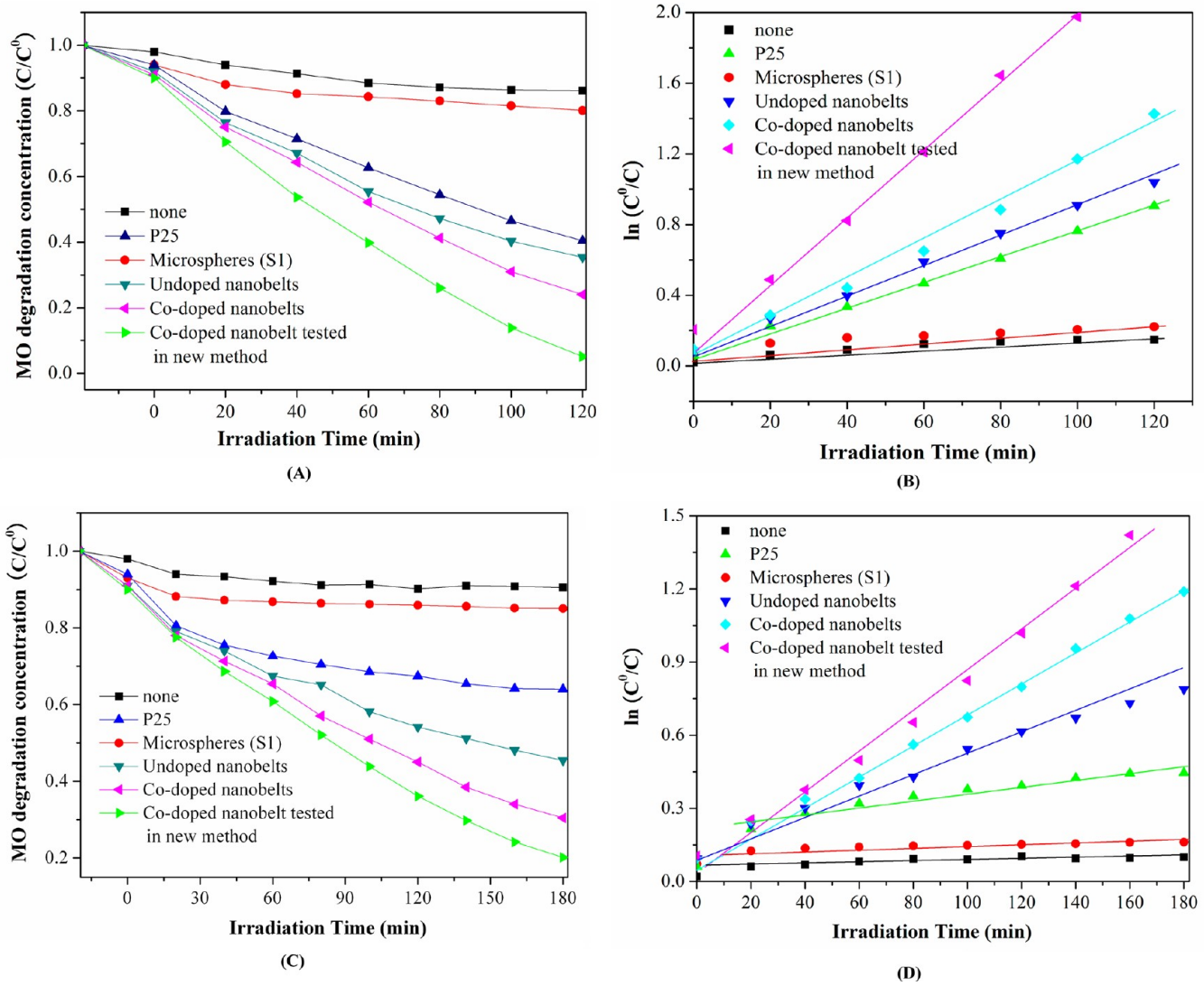

Figure 8. Temporal course of the decrease in the MO concentration (A) and ln (C^0/C) (B) with UV light irradiation time; (C) temporal course of the decrease in the MO concentration and (D) ln (C^0/C) with visible-light irradiation time.

by the BJH pore size distribution curves of the samples, the BJH pore size distribution curves of the nanobelts show a narrow normal distribution between 2.0 and 3.0 nm, and the pore size distribution centers at about 2.5 nm, which can be attributable to the solvothermal treatment at a low temperature for a long time (180 °C for 72 h). So the pore size is smaller than that of the precursor microspheres (about 3.5 nm), whereas the surface area is larger than that of the precursor microspheres. These results indicate that the nanobelts have larger amount of the wormhole-like mesopores structure (small pores).

3.5. Measurement of Light Absorption by UV−Vis Spectrophotometer. The optical band gap of the TiO_2 products was tested by an UV−vis optical absorbance spectroscopy. Figure 6 shows the UV−visible spectra of the samples in the wavelength range of 200−800 nm. It can be seen that for the undoped TiO_2 nanobelts, the absorption spectrum is cut off at ~380 nm, while for the N−F codoped nanobelts, an add-on shoulder is imposed onto the cutoff edge of the absorption spectrum, which leads to a shift of the absorption from 380 to 450 nm. By applying Tauc's equation, the optical band gap energy (E_g) of the as-synthesized products can also be calculated. Using Tauc's formula $[(Ah\nu) = B(h\nu - E_g)^n]$, the relationship between the absorption coefficient and the incident photon energy of semiconductors can be obtained, where A is the absorption coefficient, $h\nu$ is the photon energy, B is a constant and n is a value that depends on the nature of the electronic transition responsible for the absorption (n = 1/2 for direct transitions and n = 2 for indirect transitions). The inset curves in Figure 6 exhibit the optical band gaps of the N−F codoped nanobelts (obtained by extrapolation) and their values are 3.17 and 3.27 eV for the doped and undoped TiO_2 nanobelts respectively, which are very close to the optical band gap values as reported in the literatures.[34,35] The UV−visible absorption results indicate that the red shift of the optical energy gap as seen in Figure 6 should result from the solvothermal treatment. Such light absorbance enhancement in the near-UV region and in the visible light range is consistent with the yellow color characteristic of the N−F codoped TiO_2 nanobelts. That is to say, the extension of the light absorption from the UV to the visible range should be ascribed to the contribution of the doped nitrogen atoms and oxygen vacancies in TiO_2 lattice, the interstitial nitrogen atoms induce the local states near the valence band edge and thus the oxygen vacancies

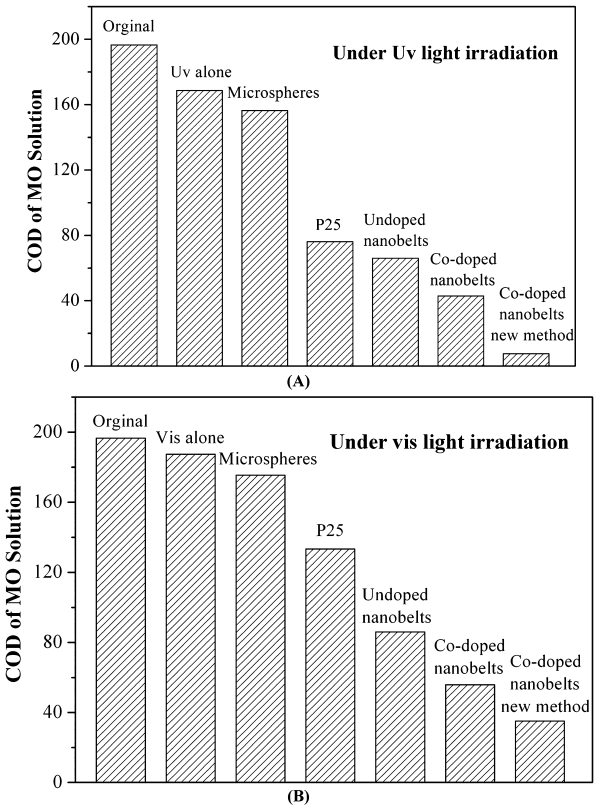

Figure 9. COD removal of the MO solution after the photocatalytic degradation in different conditions.

give rise to the local states below the conduction edge. Such an excitation from the local states to the conduction band is consistent with the "add-on shoulder" of the absorption edge of the UV−visible spectrum as reported in ref 6.

3.6. Evaluation of Photocatalytic Activities. Photocatalytic decomposition of the MO aqueous solution has been extensively studied and some possible mechanisms have been approbated by previous studies.[6,32] A scheme of possible mechanism is shown in Figure 7, showing the possible reactions that can occur in photocatalysis process. When the semiconductor is excited under light irradiation with greater energy than its band gap energy, it will cause the formation of the hole−electron pair in the semiconductor.[33] The reactions may occur as follows (Figure 7-1)

$$TiO_2 + h\nu \rightarrow e^- + h^+ \quad (1)$$

$$e^- + h^+ \rightarrow \text{energy} \quad (2)$$

Subsequently, redox reactions can occur superoxide ions and hydroxyl radicals which are nonselective strong oxidizing agents, Hole (h^+) with high activity may react with H_2O or hydroxyl groups adsorbed on the surface of the semiconductor, the formed hydroxyl radicals also have strong oxidizing activity (Figure 7-2).

$$h^+ + H_2O \rightarrow \cdot OH + H^+ \quad (3)$$

$$h^+ + (-OH) \rightarrow \cdot OH \quad (4)$$

Electron (e^-) may react with O_2 absorbed on the surface (Figure 7-3, -4)

$$O_2 + e^- \rightarrow \cdot O_2^- \quad (5)$$

$$\cdot O^{2-} + 2H_2O \rightarrow \cdot OOH + 2OH^- \quad (6)$$

$$2\cdot OOH \rightarrow O_2 + H_2O_2 \quad (7)$$

$$\cdot OOH + H_2O + e^- \rightarrow H_2O_2 + OH^- \quad (8)$$

$$H_2O_2 + e^- \rightarrow \cdot OH + OH^- \quad (9)$$

$$H_2O_2 + h\nu \rightarrow 2\cdot OH \quad (10)$$

Hole (h^+) and electron (e^-) can react with the dye molecule in favor of its degradation directly and following mineralization (Figure 7-5, -6, -7).

$$\cdot O_2^- + \text{MO} \rightarrow \text{degraded product} \quad (11)$$

$$\cdot OH + \text{MO} \rightarrow \text{degraded product} \quad (12)$$

The photocatalytic degradation of the MO aqueous solution can be regarded as a pseudofirst-order reaction. Therefore, its kinetics can be expressed by the following formula

$$C = C^0 e^{-kt} \quad (13)$$

where k (min^{-1}) is the degradation rate constant, C is the MO concentration at reaction time t, and C^0 is the initial MO concentration. According to eq 13, the degradation rate constant of the samples can be calculated and their values are listed in Table 2.[36] It can be seen from Table 2 that the value of the degradation rate constant (k) of the F−N codoped TiO_2 nanobelts is up to 0.0093 min^{-1}, which is bigger than that of P25 (0.0067 min^{-1}). The value of the degradation rate constant (k) of he F−N codoped TiO_2 nanobelts while test in new method is further increased up to 0.0165, which is almost three times as that of P25.

In the process, the MO can interact with the photogenerated holes in the valence band (VB) of the semiconductor and provides a direct chemical reaction between the dye and the

Table 3. COD of Organic Substrates Using Different Photocatalysts

	COD of the MO solution with respect to irradiation time (mg/L) (initial COD = 196.56 mg/L)									
	UV light irradiation time (min)						visible-light irradiation time (min)			
photocatalyst	20	40	60	80	100	120	40	100	140	180
none	184.42	179.07	173.20	170.57	168.89	168.59	187.11	186.66	184.69	184.36
microspheres (S1)	172.33	166.68	164.82	162.22	159.16	156.39	178.71	176.88	176.14	175.40
P25	155.75	138.94	120.97	104.49	88.41	76.11	160.05	158.67	146.27	133.37
undoped nanobelts	148.85	130.06	106.46	89.78	75.84	65.94	142.97	123.81	105.59	86.04
co-doped nanobelts	140.06	124.36	99.87	77.79	57.02	42.89	138.52	97.46	72.12	55.91
co-doped nanobelts in new testing method	137.00	102.84	74.84	47.04	22.35	7.62	133.18	83.02	54.49	35.07

dx.doi.org/10.1021/am3019965 | ACS Appl. Mater. Interfaces 2012, 4, 6816−6826

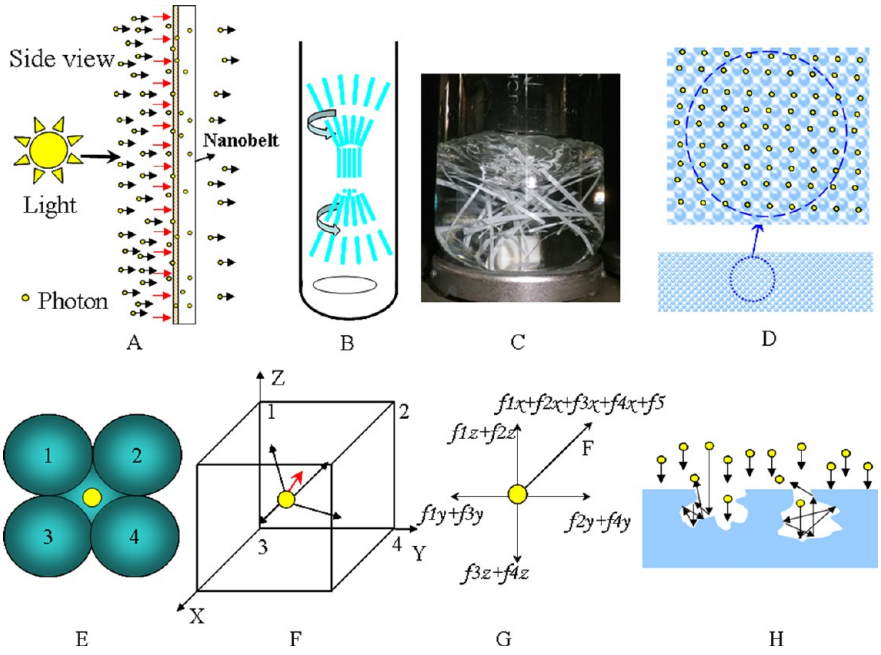

Figure 10. Schematic drawing of the photocatalytic process of the nanobelts in the new testing method.

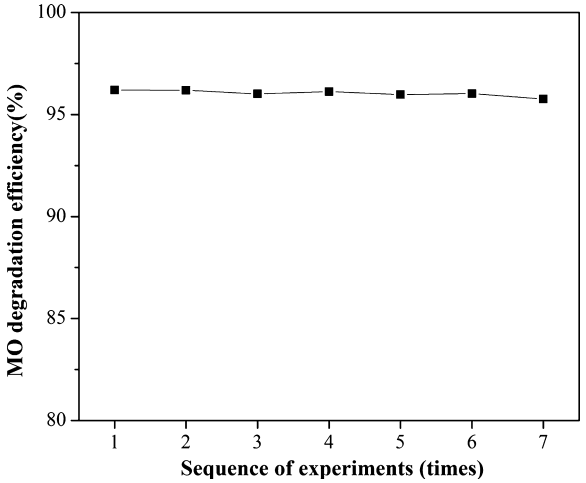

Figure 11. MO photocatalytic degradation efficiency of repeating experiments for the N−F codoped TiO_2 nanobelts (experiment condition, 20 mg/L initial concentration of the MO, scotch tape covered with photocatalysts; and irradiation time, 120 min).

photocatalyst. The photocatalytic activities of our products were evaluated by monitoring the decomposition of the MO aqueous solution under UV and visible light irradiation and are shown in Figures 8. To confirm the MO decomposition, we also measured the oxygen equivalent of the organic matter of a sample, i.e., chemical oxygen demand (COD). Results indicate that a decrease in COD values for the organic compounds (MO) can be clearly observed from Figure 9 and the decrease in COD values confirms the degradation of the organic compounds. Especially, the organic compounds are found to show the highest decrease in COD values by using the codoped nanobelts photocatalyst under both visible light and UV irradiation as shown in Figure 9. The decrease in COD values for the photocatalyst during the decomposition is also listed in Table 3.

It can be noted that a trend of the photocatalytic activity is as follow order: codoped nanobelts tested in new method > codoped nanobelts > undoped nanobelts > P25 > microspheres> none. The microspheres (S1) and the nanobelts regardless of codoped and undoped all have larger surface area, so there is a little decrease of the MO concentration at the beginning. As compared to the photocatalytic activity of P25 and the precursor microspheres (S1), the nanobelts exhibit the higher activity under both visible light and UV irradiation. There are many reasons to affect the photocatalytic activity, as mentioned in the section 1: (i) enhanced visible light scattering and absorption;[6,8,9] (ii) rapid and diffusion-free electron transport along the longest direction;[6,9−11] (iii) the high degree of crystalline and the low number of grain boundaries;[6,9] (iv) smaller pore size and larger surface area. In addition, the codoped nanobelts show an enhanced activity as compared to the undoped ones, it is probably related to that the N−F codoping induces oxygen vacancy and leads to the red shift of optical energy gap. The doped N atoms in TiO_2 improve its visible light adsorption and increase the number of photons to take part in the photocatalytic reaction, and thus enhance the overall photocatalytic activity.[6,14,16,17] The doped-F atoms lead to the enhancement of the surface acidity, which can increase the adsorption of the reactant and thus further enhance the photocatalytic activity.[23,29−31] The F-doping might lead to the formation of new active sites and hydroxyl radicals (OH•). That is to say, the fluorinated TiO_2 facilitates the formation of the hydroxyl radicals[37,38] and the hydroxyl radicals (OH•) are generally regarded as an important active species to initiate a photocatalytic reaction.

It is interesting to note that the photocatalytic activities of the N−F codoped nanobelts photocatalysts are obviously enhanced when tested in the new method. To understand it better, a schematic drawing for the photocatalytic process of the nanobelts in the new testing method is shown in Figure 10. The photons can continuously irradiate the nanobelts in the new testing method as shown in Figure 10A (the scheme drawing for the photocatalytic process in the normal method is shown

dx.doi.org/10.1021/am3019965 | ACS Appl. Mater. Interfaces 2012, 4, 6816−6826

in Figure 10B, C). A model of the nanobelts as shown in panels D and E in Figure 10 is given, where the nanobelts are composed of small grains and there are wormhole-like mesopores at the interface of them. As we know, for each namable, the stoichiometry is preserved and no saturation of dangling bonds or charge embedding is applied. The interior grains exist equal attraction with the surrounding grains in all directions, but the surface grains does not so, thus, near the surface will form a force field and its direction points inside the nanobelts (Figure 10F, G). The photons from irradiated nanobelts, once enter into the scope of this force field will be absorbed on the surface by this force field (F = f1+f2+f3+f4+f5, the forces field (f1+f2+f3+f4) are from the grains nearly the photons, and f5 corresponds to other grains (as shown in Figure 10G). As we can see from this model, when the photons enter the pore like prison, the "Prison Break" is not easy for the photons to escape as shown in panels D and E in Figure 10, and even more difficult than the one as shown in Figure 10H. That is to say, it is possible to enhance the absorption of the photons, the photons may collide with the nanobelts and thus the energy exchange exists in this collision. Since the photons can irradiate the nanobelts continuously in the new testing method, thus more photons can react on the surface and in the interfaces of the nanobelts, also stimulate the formation of the hole−electron pair in the semiconductor (this process is as shown in Figure 7-1). Furthermore, considering that there are many small pores on the surface of the nanobelts, they may provide the reaction field, which can increase the photocatalytic activity. In addition, there are many small pores in the nanobelts. These pores can provide the reaction field, which can mainly increase the photocatalytic activity.

3.7. Stability of the New Testing Method. A stability of the N−F codoped TiO_2 nanobelt photocatalysts tested by the new testing method was also investigated by repeating a measurement of the photocatalytic degradation of the MO. In our study, the scotch tape covered with the N−F codoped TiO_2 nanobelt photocatalysts, which have no any treatment after each experiment, are used to confirm the stability of the new testing method. It is significant to find that after seven repeating experiments for photocatalytic degradation of the MO, the degradation efficiency of the nanobelt photocatalysts is rather stable and can remain above 90%, as shown in Figure 11.

4. CONCLUSIONS

The N−F codoped TiO_2 nanobelts with anatase phase structure have been successfully prepared by the solvothermal method, which employs amorphous titania microspheres as the precursor. Results indicate that the N−F codoped nanobelts possess larger amount of the wormhole-like mesopores prison, and the "Prison Break" is not easy for the photons to escape, so the photocatalytic activity of the nanobelts shows highly enhanced, which is also probably related to that the N−F codoping induces oxygen vacancy and leads to the red shift in optical energy gap. In addition, when the measurement of the photocatalytic activity is in the new testing method, the photocatalytic activities of the nanobelts are further enhanced because more photons are captured by the nanobelts to stimulate the formation of the hole−electron pair, which this testing method gives us a new way to enhance the photocatalytic activity of the nanobelt photocatalyst.

■ ASSOCIATED CONTENT

Ⓢ Supporting Information

Additional figures and information (PDF). This material is available free of charge via the Internet at http://pubs.acs.org.

■ AUTHOR INFORMATION

Corresponding Author

*Tel.: +86-29-82668679. Fax: +86-29-82668794. E-mail: wxque@mail.xjtu.edu.cn.

Notes

The authors declare no competing financial interest.

■ ACKNOWLEDGMENTS

This work was supported by the Major Program of the National Natural Science Foundation of China (90923012 and No. 61078058), the Science and Technology Developing Project of Shaanxi Province (2012KW-11), and the Ministry of Science and Technology of China through 863-project under Grant 2009AA03Z218.

■ REFERENCES

(1) Asahi, R.; Morikawa, T.; Ohwaki, T.; Aoki, K.; Taga, Y. *Science* **2001**, *293*, 269.
(2) Aykut, Y.; Saquing, C. D.; Pourdeyhimi, B.; Parsons, G. N.; Khan, S. A. *ACS Appl. Mater. Interfaces* **2012**, *4*, 3837.
(3) Hwang, S. H.; Kim, C.; Song, H.; Son, S.; Jang, J. *ACS Appl. Mater. Interfaces* **2012**, *4*, 5287.
(4) He, Z. L.; Que, W. X.; He, Y. C.; Chen, J.; Xie, H. X.; Wang, G. F. *J. Mater. Sci.* **2012**, *47*, 7210.
(5) Pandikumar, A.; Murugesan, S.; Ramaraj, R. *ACS Appl. Mater. Interfaces* **2010**, *2*, 1912.
(6) Wang, J.; Tafen, D. N.; Lewis, J. P.; Hong, Z. L.; Manivannan, A.; Zhi, M. J.; Li, M.; Wu, N. Q. *J. Am. Chem. Soc.* **2009**, *131*, 12290.
(7) Kang, Q.; Liu, S. H.; Yang, L. X.; Cai, Q. Y.; Grimes, C. A. *ACS Appl. Mater. Interfaces* **2011**, *3*, 746.
(8) Chen, W.; Fan, Z. L.; Zhang, B.; Ma, G. J.; Takanabe, K.; Zhang, X. X.; Lai, Z. P. *J. Am. Chem. Soc.* **2011**, *133*, 14896.
(9) Wang, C. X.; Yin, L. W.; Zhang, L. Y.; Liu, N. N.; Lun, N.; Qi, Y. X. *ACS Appl. Mater. Interfaces* **2010**, *2*, 3373.
(10) Zhang, L. F.; Chandrasekar, R.; Howe, J. Y.; West, M. K.; Hedin, N. E.; Arbegast, W. J.; Fong, H. *ACS Appl. Mater. Interfaces* **2009**, *1*, 987.
(11) Hu, P. G.; Du, G. J.; Zhou, W. J.; Cui, J. J.; Lin, J. J.; Liu, H.; Liu, D.; Wang, J. Y.; Chen, S. W. *ACS Appl. Mater. Interfaces* **2010**, *2*, 3263.
(12) Zhou, W. J.; Liu, H.; Wang, J. Y.; Liu, D.; Du, G. J.; Cui, J. J. *ACS Appl. Mater. Interfaces* **2010**, *2*, 2385.
(13) Rabatic, B. M.; Dimitrijevic, N. M.; Cook, R. E.; Saponjic, Z. V.; Rajh, T. *Adv. Mater.* **2006**, *18*, 1033.
(14) He, Z. L.; Zhu, Z. F.; Li, J. Q.; Wei, N.; Zhou, J. Q. *J. Hazard. Mater.* **2011**, *190*, 133.
(15) Wang, H. Q.; Yan, J. P.; Chang, W. F.; Zhang, Z. M. *Catal. Comm.* **2009**, *10*, 989.
(16) Tafen, D. N.; Wang, J.; Wu, N. Q.; Lewis, J. P. *Appl. Phys. Lett.* **2009**, *94*, 093101/1.
(17) Chi, B.; Zhao, L.; Jin, T. *J. Phys. Chem. C* **2007**, *111*, 6189.
(18) Pan, J. H.; Zhang, X. W.; Du, A. J.; Sun, D. D.; Leckie, J. O. *J. Am. Chem. Soc.* **2008**, *130*, 11256.
(19) Yu, J. G.; Shi, L. *J. Mol. Catal. A: Chem.* **2010**, *326*, 8.
(20) Yu, J. G.; Xiang, Q. J.; Ran, J. R.; Mann, S. *Cryst. Eng. Commun.* **2010**, *12*, 872.
(21) Zhu, Z. F.; He, Z. L.; Li, J. Q.; Zhou, J. Q.; Wei, N.; Liu, D. G. *J. Mater. Sci.* **2011**, *46*, 931.
(22) Yu, J. C.; Yu, J. G.; Ho, W.; Jiang, Z. T.; Zhang, L. Z. *Chem. Mater.* **2002**, *14*, 3808.
(23) Pelaez, M.; Falaras, P.; Likodimos, V.; Kontos, A. G.; Cruz, A.A.e; la; O'Shea, K.; Dionysiou, D. D. *Appl. Catal. B* **2010**, *99*, 378.

(24) Katoh, M.; Imayama, A.; Mori, N.; Horikawa, T.; Tomida, T. *Int. J. Mod. Phys. B* **2010**, *24*, 3242.
(25) Wu, Y. M.; Xing, M. Y.; Tian, B. Z.; Zhang, J. L.; Chen, F. *Chem. Eng. J.* **2010**, *162*, 710.
(26) Chen, D. M.; Jiang, Z. Y.; Geng, J. Q.; Zhu, J. H.; Yang, D. *J. Nanopart. Res.* **2009**, *11*, 303.
(27) Li, D.; Haneda, H.; Hishita, S.; Ohashi, N.; Labhsetwar, N. K. *J. Fluorine Chem.* **2005**, *126*, 69.
(28) Li, D.; Haneda, H.; Labhsetwar, N. K.; Hishita, S.; Ohashi, N. *Chem. Phys. Lett.* **2005**, *401*, 579.
(29) Kontos, A. G.; Pelaez, M.; Likodimos, V.; Vaenas, N.; Dionysiou, D. D.; Falaras, P. *J. Photochem. Photobiol. A* **2006**, *184*, 282.
(30) Xie, Y.; Li, Y. Z.; Zhao, X. J. *J. Mol. Catal. A: Chem.* **2007**, *277*, 119.
(31) Li, D.; Haneda, H.; Hishita, S.; Ohashi, N. *Chem. Mater.* **2005**, *17*, 2596.
(32) Montoya, J. F.; Velásquez, J. A.; Salvador, P. *Appl. Catal. B* **2009**, *88*, 50.
(33) Subramanian, V.; Wolf, E. E.; Kamat, P. V. J. *Am. Chem. Soc.* **2004**, *126*, 4943.
(34) Abaker, M.; Umar, A.; Baskoutas, S.; Kim, S. H.; Hwang, S. W. *J. Phys. D: Appl. Phys.* **2011**, *44*, 155405.
(35) Abaker, M.; Umar, A.; Baskoutas, S.; Dar, G. N.; Zaidi, S. A.; Al-Sayari, S. A.; Al-Hajry, A.; Kim, S. H.; Hwang, S. W. *J. Phys. D: Appl. Phys.* **2011**, *44*, 425401.
(36) Umar, A.; Abaker, M.; Faisal, M.; Hwang, S. W.; Baskoutas, S.; Al-Sayari, S. A. *J. Nanosci. Nanotechnol.* **2011**, *11*, 3474.
(37) Minero, C.; Mariella, G.; Maurino, V.; Pelizzetti, E. *Langmuir* **2000**, *16* (6), 2632.
(38) Minero, C.; Mariella, G.; Maurino, V.; Pelizzetti, E. *Langmuir* **2000**, *16* (23), 8964.

NOTE ADDED AFTER ASAP PUBLICATION

This paper was published on the Web on November 30, 2012. Additional minor text corrections were added, and the corrected version was reposted on December 11, 2012.